Nature Communications

https://doi.org/10.1038/s41467-026-74526-7

Article in Press

# Longitudinal analysis of influenza A virus deletion-containing viral genomes reveals key determinants of co-evolutionary dynamics and interference

Received: 29 December 2025

Accepted: 9 June 2026

Cite this article as: Alnaji, F.G., Farjo, M., Goh, S.L. *et al.* Longitudinal analysis of influenza A virus deletion-containing viral genomes reveals key determinants of co-evolutionary dynamics and interference. *Nat Commun* (2026). https://doi.org/10.1038/s41467-026-74526-7

**Fadi G. Alnaji, Mireille Farjo, Shu Ling Goh, Daryl Zheng Hao Aw, Paolo Alberto Lorenzini, Tongyu Liu, Rebekah Lin-Zhen Chan, Cornelius Lee, Marco Vignuzzi & Christopher B. Brooke**

# Longitudinal analysis of influenza A virus deletion-containing viral genomes reveals key determinants of co-evolutionary dynamics and interference

Fadi G. Alnaji[1], Mireille Farjo[2], Shu Ling Goh[1], Daryl Zheng Hao AW[1], Paolo Alberto Lorenzini[1,3], Tongyu Liu[2], Rebekah Chan Lin-Zhen[1], Cornelius Lee[1], Marco Vignuzzi[1,4,5,#], and Christopher B. Brooke[2,6,#]

[1] Agency for Science Technology and Research (A*STAR), Infectious Disease Labs, Singapore
[2] Department of Microbiology, University of Illinois at Urbana-Champaign, Champaign, Illinois, USA
[3] Bioinformatics Institute (BII), Agency for Science, Technology and Research (A*STAR)
[4] Infectious Diseases Translational Research Programme, Department of Microbiology and Immunology, Yong Loo Lin School of Medicine, National University of Singapore, Singapore, Singapore
[5] Lee Kong Chian School of Medicine, Nanyang Technological University, Singapore
[6] Carl R. Woese Institute for Genomic Biology, University of Illinois at Urbana-Champaign, Champaign, Illinois, USA

#Corresponding author Christopher B. Brooke (cbrooke@illinois.edu) & Marco Vignuzzi (Marco_Vignuzzi@IDLabs.a-star.edu.sg).



**Abstract:**

Influenza A virus populations contain substantial genetic diversity. A major contributor to this diversity is the ubiquitous production of deletion-containing viral genomes (DelVGs) – viral RNAs with large internal deletions. DelVGs directly compete with wild-type (WT) genomes and have been implicated in modulating disease severity. However, the specific functional and genetic interactions between DelVGs and WT genomes remain poorly understood. To examine how DelVGs and WT genomes co-evolve, we serially passage influenza A virus and use next-generation sequencing to build a longitudinal profile of DelVG emergence and dynamics. Highly diverse repertoires of DelVGs observed in early passages undergo sharp contractions in overall diversity, leaving only one or two DelVGs that persist at high frequency. We also identify a recurring substitution that significantly enhances DelVG replication and interference potency. These findings reveal DelVGs to be dynamic genomic elements that are subject to unique selection forces and actively shape viral population dynamics.

**Introduction:**

Influenza A viruses (IAV) are negative-stranded, segmented RNA viruses responsible for yearly seasonal epidemics and occasional global pandemics. IAV populations exist as highly diverse swarms of genetically and phenotypically heterogeneous particles [1]. One of the most well-known contributors to viral population heterogeneity are defective interfering particles (DIPs): virions that carry one or more viral gene segments containing large internal deletions, also known as deletion-containing viral genomes (DelVGs) [2,3]. Because these deletions occur within essential viral genes, DelVGs cannot replicate independently, and depend on co-infection with WT virus to replicate.

IAV DelVGs are ubiquitous in both *in vitro* and *in vivo* infection models [4–8], as well as in clinical samples [9–12]. Importantly, the abundance of DelVGs within clinical samples correlated negatively with infection severity in one study [12], emphasizing the need to better understand how DelVGs can modulate infection dynamics.

It has been known for decades that DelVGs can interfere with WT replication, leading to DelVGs outcompeting WT virus and numerically dominating viral populations under the right conditions [4,13]. The mechanisms by which this occurs are not fully understood, though competition with WT genomes for replication and packaging [14,15] and stimulation of the innate immune response [16,17] have all been proposed. We recently demonstrated that IAV DelVGs are actually replicated and packaged less efficiently than WT genomes over the course of a single replication cycle, raising questions about how they are able to outcompete WT virus over multiple generations [18].

To better understand the processes underlying DelVG accumulation and the evolutionary interplay between DelVGs and WT genomes within complex viral populations, we serially passage IAV for 72 passages under sustained high MOI conditions and examine DelVG dynamics using next-generation sequencing (NGS). This approach yields a detailed profile of the competition and co-evolution between DelVGs and WT genomes and reveals specific molecular features that govern the competitive success of DelVGs.

**Results:**

**Von Magnus oscillations and genome-wide DelVG distributions are highly reproducible.**

To better understand how WT genomes and DelVGs interact and co-evolve within viral populations, we serially passaged recombinant A/Puerto Rico/8/1934 (rPR8) in two parallel replicate lineages under sustained high MOI conditions in MDCK cells. Both lineages were initiated from the same parental rPR8 population at an MOI of 10 $TCID_{50}$ /cell. Each passage was allowed to proceed for 18-20 hours, at which point half of the supernatant was used to infect the next passage while the other half was aliquoted and frozen.

To measure the accumulation of DIPs (packaged DelVGs) during passage, we measured infectivity by Tissue Culture Infectious Dose 50% ($TCID_{50}$ ) assay, physical particles by hemagglutination (HA) assay, and calculated particle:infectivity ratios for each passage (**Fig 1A**) by dividing hemagglutination unit (HAU) titers (proxy for total particle counts) by corresponding $TCID_{50}$ values for each sample. In both lineages, particle:infectivity ratios increased nearly five orders of magnitude over the first 7-9 passages, (compared with a ratio ~10 for parental virus stock), suggesting a massive accumulation of DIPs relative to WT virus. Particle:infectivity ratios in both lineages crashed back to ~10 over the next few passages, beginning an oscillatory pattern that continued throughout the 72-passage experiment. This oscillation pattern (often referred to as the “Von Magnus effect") has been described many times before [4,18–20], and our data indicates that this dynamic can be maintained stably within IAV populations for at least 100+ generations (assuming 2 viral generations per 18 hour passage).

To identify the specific DelVGs that emerged within the passage populations, we used our optimized NGS-based pipeline [6] to characterize the deletion junctions in several representative passages with high particle:infectivity ratios (**Fig S1A**)**.** Consistent with previous reports, hundreds of diverse DelVGs were detected across all segments except NS, with the majority derived from the polymerase segments (**Fig 1B**). To further investigate the reproducibility of DelVG formation and accumulation, we initiated 6 additional replicate passage populations from

the same parental population as lineages 1 and 2. We analysed the DelVG junctions in the polymerase *PB2* segment present at passage 34 and observed minimal overlap in the specific DelVG deletions across the eight replicate lineages (**Fig 1C, Fig S1B**). This strongly suggests that while DelVG formation is reliably concentrated within well-defined hotspots and segments, the specific deletion junctions that form appear highly stochastic within those hotspots.

**DelVG diversity decreases over repeated passaging**

We observed a reduction in both the numbers of unique deletion junctions (across all segments) and the numbers of DelVG-mapping NGS reads (in all segments except *PB2* and *PB1*) in later passages (**Fig 1B**). To look at this another way, we plotted the WT:DelVG ratios for segments 1-3 (based on NGS read counts) across several passages where particle:infectivity ratios peaked, demonstrating that DelVG abundance dropped off after the initial expansion for some but not all segments (**Fig 2**). This was not due to any variation in overall segment abundance, as WT versions of the three polymerase segments remained at similar relative abundances throughout the experiment (**Fig S2A**).

While DelVG abundance remained high for some segments but not others, the diversity of individual junctions (based on Shannon entropy calculations) was sharply reduced for the polymerase segments (**Fig 2**). Thus, even when DelVG abundance remained high for a given segment, it was due to a small number of specific deletions. Interestingly, the dramatic changes in DelVG segment distributions and genetic diversity that occurred over the course of the experiment did not disrupt the Von Magnus oscillation pattern, suggesting that the general pattern of WT-DelVG interactions was largely independent of the specific makeup of the DelVG population.

**DelVG competition dynamics vary across genome segments**

To better understand the processes of competition and selection that shaped the DelVG populations during passages, we visualized the dynamics of individual DelVG junctions in relation to other DelVGs (**Fig 3**). DelVG dynamics differed substantially between genome segments but were generally similar between the two passage lineages.

For the *PB2* segment, we observed the expansion of a diverse population of hundreds of distinct DelVGs in both lineages over the first ~20 passages, followed by 1-2 specific DelVGs slowly and steadily taking over the population by the last passage (**Fig 3**). Notably, the three *PB2* DelVG junctions that collectively took over lineages 1 and 2 had highly similar junction coordinates (129_2092, 128_2094, and 129_2096) (**Fig S2B**), suggesting that specific junction attributes may be associated with competitive success. Importantly, other DelVGs present at higher initial frequencies declined while these became dominant indicating that early abundance or emergence timing alone does not explain competitive outcomes.

The *PB1* and *PA* segments showed similar initial expansions of diversity; however, the frequencies of individual deletions relative to each other appeared more stable, with no individual junctions outcompeting the others. Unlike *PB2*, DelVGs derived from *PB1* (in lineage 1) and *PA* (in both lineages) largely disappeared after passage ~50. *HA* DelVGs exhibited a rapid expansion of diversity, like the polymerase segments, but also exhibited a much more rapid collapse, largely disappearing from lineage 1 by passage 20 and lineage 2 by passage 40. *NA* DelVGs similarly peaked early and became largely absent after passage 40. Dynamics in the *M* segment were unique, in that DelVGs did not begin to accumulate until much later (first

peaks around passage 20). The expansion and contraction dynamics of individual *M*-derived DelVGs also appeared to be more stochastic than those observed for other segments.

Altogether, our data suggest that DelVGs from different segments are subject to distinct evolutionary dynamics and that evidence of strong selection/competition dynamics is only clearly apparent in the *PB2* segment. The near-total disappearance of DelVGs from some segments and lack of emergence of new DelVG junctions in later passages also suggest that viral populations can become resistant to invasion by *de novo*-generated DelVGs.

**Deletion size and reading frame do not determine DelVG success**

DelVG length has been suggested to govern competitive success, with shorter DelVGs thought to outcompete longer DelVGs and WT genomes [21]. Similarly, the specific translation products of DelVGs have also been suggested to mediate interference with WT replication [22]. We thus asked whether deletion size or post-deletion translation reading frame correlated with DelVG competitive success in our dataset. We compared DelVG sizes for segments 1-3 across four DIP-rich passages from both lineages (P8, P21, P34, P72) (**Fig S3A**). No major shift in deletion length was observed across passages for any segment. While statistical differences were detected in some comparisons, deletion length distributions remained broadly overlapping with no consistent directional trend. Notably, the range of deletion sizes observed at early passages was largely retained at later passages, indicating that deletion size is not a primary determinant of DelVG competitive success.

We also found no evidence for enrichment of specific translation frames (**Fig S3B**). Although there was a notable bias toward the +0 frame at passage 72 in L1, this was not seen in lineage 2 and may simply be an artifact of the small number of DelVG junctions remaining by passage 72. These observations suggest that under our experimental conditions, DelVG competitive dynamics cannot be simply explained by deletion size or post-deletion translation reading frame.

**Reconstitution of DelVG competition dynamics**

It was possible that the complex competition and evolutionary dynamics we observed in our passage experiment were largely stochastic and were thus not reproducible. To test the reproducibility of the DelVG dynamics we observed, we attempted to recapitulate the competition dynamics we observed in the original experiment using recombinant, clonal DIP populations.

We selected three DelVGs from passage lineage 1, based on their competitive dynamics over time: DI250, which outcompeted all other DelVGs; DI143, which was less competitive but still maintained at detectable frequencies through most of the experiment; and DI289, which was rapidly outcompeted and disappeared (**Fig 4A**). We generated clonal recombinant DIPs encoding these specific DelVGs using reverse genetics, and developed qPCR primer probe sets that could distinguish between the individual DelVGs (**Fig S4A-D**).

Next, we performed competition experiments in which MDCK cells were co-infected with each of the three DIPs at an input of 1 *PB2* genome equivalent (*PB2*-GE) per cell, together with WT PR8 at 10 *PB2*-GE/cell, across three independent lineages. This input ratio was chosen to provide abundant WT helper virus while establishing conditions in which the three DelVGs competed both with WT *PB2* and with one another. Control infections lacking WT virus confirmed that the recombinant DIPs did not replicate, as expected **(Fig S4E)**. We then performed 16

undiluted passages of these populations and quantified the absolute abundances of DI250, DI143, DI289, and WT *PB2* at each passage by RT-qPCR **(Fig. 4B).**

In broad strokes, these competition experiments reproduced the expected WT-DelVG dynamics, where the DelVGs outcompete the WT virus over the first several passages, before being overtaken by WT virus during the final passages. When we examined the dynamics of individual DelVGs, however, these conditions failed to recapitulate the specific inter-DelVG competition dynamics observed in the original experiment. While DI250 dominated in the original passage experiment, it was consistently outreplicated by DI143 and DI289 in all replicate experiments. Across the three replicates, DI143 consistently replicated to higher titers than the other DelVGs. These data demonstrated that DelVG competition dynamics can be highly reproducible across independent experiments, at least under artificial, reductionist conditions, suggesting that individual DelVGs have intrinsic competition phenotypes that can drive reproducible dynamics. However, these results also indicated that our competition experiments failed to recapitulate key aspects of the original passage experiments that gave rise to the dynamics we observed.

**Emergence of DelVG-associated SNPs during WT/DelVG co-evolution**

Our inability to reproduce the DelVG competition hierarchy observed in the original experiment using recombinant DIPs suggested that we were failing to reproduce a key driver of the original dynamics. We hypothesized that competition between WT and DelVGs may have driven the emergence of substitutions that influenced WT/DelVG dynamics. To test this, we developed a bioinformatics approach to distinguish the reads of the selected DelVGs from other DelVGs and WT in the sequencing data generated from the long passage experiment, aiming to identify single nucleotide polymorphisms (SNPs) that emerged within DelVGs over the course of passaging (**Fig 5**).

In lineage 1, a single SNP rose to high frequency within the dominant DelVG DI250 after passage 15 (**Fig 5**), changing adenine to guanine at position 94 of the (+) strand sequence (hereafter referred to as A94G), which coded a threonine-to-alanine substitution at position 23 of PB2. This same SNP also arose to high frequency within one of the dominant DelVGs in lineage 2, DI248, suggesting that this SNP may confer some advantage during WT/DelVG co-evolution. Interestingly, this SNP was absent from WT *PB2*-derived reads. When introduced into WT PR8 by reverse genetics, the A94G substitution markedly attenuated viral replication, and rapidly reverted to WT (**Fig 6A**). These findings suggest that while A94G may be tolerated – or even advantageous – within DelVG backgrounds, it is maladaptive in WT viruses, underscoring its context-dependent effect on viral fitness. Consistent with this, A94G nevertheless rose to high frequency in competitive DelVGs in both passage lineages (**Fig 5**) despite being highly attenuating in WT PR8.

**A94G enhances DelVG replication kinetics and inhibitory activity**

To better understand the effects of the A94G mutation on DelVG function, we measured the relative abilities of DI250 and DI250:A94G to interfere with viral polymerase activity in a minigenome replicon assay (**Fig 6B, left panel**). In this assay, we expressed the components of the viral polymerase complex from plasmids in cells, along with a firefly luciferase-encoding reporter RNA derived from the viral *NS* gene segment and measured the accumulation of firefly luciferase signal as a surrogate for viral polymerase activity. We found that DI250 inhibited polymerase activity, relative to a WT PB2 control, and that this inhibitory effect was significantly increased for DI250:A94G.

To assess whether the outcomes observed in our minigenome assay were recapitulated during viral infection, we re-generated DI250 and newly generated DI250:A94G, producing DIP clonal populations of both (**Fig S5A**). Next, we used these DIPs to conduct a competition assay at a WT:DIP ratio of 1:10 *NP*-GE/cell (**Fig 6B, right panel**). Our finding mirrors the minigenome data, offering further support that A94G enhances the interfering capacity of DI250.

Finally, to directly examine the effects of A94G on DelVG competition dynamics, we co-passaged WT PR8 along with either DI250 or DI250:A94G for 14 passages and measured both DelVG abundance (by RT-qPCR) and fully infectious particle yield (by $TCID_{50}$ assay). The relative abundance of DI250:A94G increased earlier and rose to a higher magnitude compared with DI250 (**Fig 6C; replicate 2 shown in Fig S5B**). *NP* copy number dynamics (**Fig S5C**) indicate that the increased DI:*NP* ratio reflects a combination of enhanced DI replication and suppression of *NP* accumulation by the mutant. Consistent with this, we observed that fully infectious virus titers declined more rapidly in the presence of DI250:A94G compared to DI250. Importantly, Sanger sequencing at late passages confirmed the persistence of A94G (**Fig S5D**), indicating that it is stable within DelVGs. This suggests that the emergence of this substitution enhances the competitive advantage of DI250 and likely facilitated the evolutionary success of the DI250 genotype during long-term passaging.

**A94G has no clear effect on packaging**

To better assess the effects of A94G on DelVG replication and packaging, we performed an independent passaging experiment in which WT PR8 was co-passaged with either clonal DI250 or DI250:A94G individually, using an input of 0.1 MOI for each DIP and 1 MOI WT (*PB2*-GE/cell) in MDCK cells, with duplicate lineages for each condition. Quantitative tracking began at P3, when both DelVGs were reliably detectable at comparable levels across lineages, providing a common baseline (**Fig 7**). From P3 onward, DelVG levels were measured in cells (6 hpi) and in virions up to P5 by junction-specific qPCR, with *NP* assayed in parallel as a reference. This allowed us to independently examine replication and packaging, enabling direct comparison of the two DelVGs under matched conditions. DI250:A94G consistently showed higher intracellular and virion-associated copy numbers than DI250 (**Fig 7A**), together with an increased DelVG/*NP* ratio (**Fig 7B**) (at comparable *NP* (**Fig S5E**)), suggesting higher replication efficiency.

To determine whether the observed replication advantage also extends to packaging, we calculated the packaging index across passages P3–P5 and found similar ratios between DI250 and DI250:A94G across both passage windows and replicates (**Fig S5F**).

We then co-transfected both DelVG plasmids at a 1:1 ratio together with the seven remaining PR8 plasmids and a *PB2* mRNA–expressing plasmid in triplicate (**Fig S6A**) and quantified the packaged DelVG sequences by Nanopore amplicon sequencing. This setup maintains a constant PB2 protein supply, eliminates competition with the full-length *PB2* genome, equalizes the initial vRNA input from plasmids, and largely minimizes replication.

Before analyzing these samples, we validated our quantification approach using predefined plasmid mixtures containing both DelVGs (**Fig S6B**). Finally, sequencing of virion RNA from the 1:1 co-transfection revealed that both DelVGs were packaged in equal proportion, with a consistent ~50:50 ratio across all three replicates (**Fig 7C**).

Together, these results indicate that both DelVGs are packaged with comparable efficiency when replication and WT competition are controlled, and that A94G enhances the replication and intracellular competitive advantage of DI250, accounting for its sustained dominance over time.

**Discussion:**

The effects of DelVGs on the fitness and phenotypes of influenza virus populations remain very poorly understood. One way to explore the interactions between WT genomes and DelVGs is to examine their co-evolutionary dynamics over time within IAV populations. Here, we used NGS to detail the complex dynamics of DelVGs during extended *in vitro* passaging under sustained high MOI conditions. By tracking individual DelVGs and WT genomes within parallel populations over 72 passages, we generated a high-resolution profile of intra-population DelVG competition. This approach, combined with *in vitro* competition assays using recombinant DelVGs, allowed us not only to identify aspects of WT/DelVG dynamics that are highly reproducible versus those that are more stochastic, but also a DelVG-specific mutation that had a profound effect on DelVG replication and competition with WT genomes.

We observed clear inter-DelVG competition primarily within the *PB2* segment and, to a lesser extent, in other polymerase segments, whereas DelVG dynamics within the non-polymerase segments were more consistent with random drift. A parsimonious explanation is that deletions in polymerase segments render virions replication-deficient, enforcing strict dependence on WT complementation; under high MOI, such *PB2*-derived DelVGs can exploit limiting pools of the polymerase and NP, driving repeatable selective sweeps. By contrast, DelVGs in non-polymerase segments can still be replicated as RNAs in coinfected cells but typically generate semi- or non-infectious progeny [23] and face strong packaging bottlenecks that limit their potential for direct competition. This interpretation is supported by mechanistic models showing that DelVGs gain a competitive edge by sequestering limiting polymerase and NP, with the models also predicting greater competitiveness for polymerase-segment DelVGs [24,25].

Our data indicate that A94G confers an advantage to *PB2* DelVGs primarily at the replication level, which is likely to contribute to its strong interfering activity. While the precise mechanism remains to be elucidated, we did not observe any bias toward in-frame deletions; however, DI250 happens to be in-frame. This raises the possibility that its encoded protein may play a role, especially given recent evidence suggesting that DelVG-derived proteins can act as dominant-negative inhibitors in cell culture [22].

Our experiments were performed in MDCK cells under controlled MOI conditions, which may not fully capture the dynamics of DelVG replication and packaging in other cell lines or in vivo. Moreover, our quantification relied on junction-specific qPCR of two selected DelVG clones, potentially overlooking contributions from other variants present in natural infections. While our design allowed replication to be decoupled from packaging, we cannot exclude additional factors such as RNA stability, host cell type, or segment interactions influencing the relative success of DI250:A94G over DI250. In addition, closely spaced junctions (e.g., 129_2092, 128_2094, and 129_2096) were resolved as distinct DelVG species by our NGS pipeline, supported by reproducible read counts and manual inspection of individual reads, although minor alignment ambiguity cannot be fully excluded. Future studies in primary human airway cells or animal models, and structural analyses of DelVG junctions, will be needed to generalize these findings and pinpoint the molecular basis of the observed differences.

Despite the limitations inherent in the cell culture system used here, our data reveal broader principles of DelVG population dynamics that may be relevant *in vivo*. We expect that the 72 serial passages we performed correspond to roughly 200-250 generations in our system (assuming ~3 replication cycles per passage). This long-term passaging approach was intended to amplify evolutionary dynamics that may be occurring more subtly over the timeframe of natural acute infections, which last anywhere from a couple days to a couple weeks [26]. This timeframe would be sufficient for the initial expansion and contraction of DelVG populations that we observed *in vitro*, and potentially the emergence of adaptive substitutions like A94G, but is almost certainly insufficient to support the establishment of Von Magnus oscillations or other complex behaviours observed in late passages. That said, the virus can establish long-term persistent infections in immunocompromised individuals where viral generation times can approach those of our experimental approach [27]. Under these conditions, we would expect that similar complex WT/DelVG co-evolutionary dynamics would occur and could potentially affect broader infection dynamics. Our findings also have relevance for understanding the potential use of exogenous DelVGs as therapeutics [28], as they both suggest a specific route to optimization of the therapeutic anti-viral potential of DelVGs, and highlight the importance of intra-population co-evolutionary dynamics as a major determinant of therapeutic DelVG success.

Prior studies have established how DelVGs shape infection by mapping deletion architectures that drive strong interference in arboviruses (ZIKV, CHIKV) and identifying DelVG-embedded features that heighten innate signaling in paramyxoviruses [29–31]. Complementary evidence from plant RNA viruses shows that even single-nucleotide changes within DelVG RNAs can modulate their competitive behavior, underscoring that DelVG performance can hinge on fine-scale sequence variation and not only on deletion endpoints [32–34]. Building on and integrating these insights, we show in influenza A that a SNP inside a *PB2*-derived DelVG repeatedly rose to high frequency over ~72 serial high-MOI passages, enhanced DelVG competitive success, and more strongly suppressed WT replication, while the same change was lethal in the WT background with evidence of reversion pressure. To our knowledge, this is the first demonstration in influenza that a minimal point change within *a bona fide* DelVG can tune interfering capacity and expose antagonistic pleiotropy *i.e.* decoupled fitness optima for DelVG versus WT genomes.

Altogether, these results illuminate the co-evolutionary dynamics that govern DelVG dynamics within IAV populations and point towards actionable approaches for engineering interference-optimized DelVGs for therapeutic purposes.

**Methods:**

**Cells and viruses**

MDCK and HEK293T cells were maintained in MEM (Gibco) supplemented with GlutaMAX and 8.3% FBS (Seradigm) at 37 °C, 5% $CO_2$. Recombinant A/Puerto Rico/8/1934 (PR8) was rescued in HEK293T cells using the canonical 8-plasmid influenza reverse-genetics system [35]. Undiluted rescue supernatant was transferred directly onto MDCK cells, and supernatants were collected at the first appearance of cytopathic effect to produce seed stocks. Working virus stocks were then prepared by infecting MDCK cells with seed stock at an MOI of 0.0001 $TCID_{50}$ per cell (to limit DelVG accumulation) and harvesting at 48 hpi. Supernatants were clarified at 3,000 rpm for 5 min and aliquoted (0.5 mL) for storage at −70 °C.

**Serial virus passage**

Confluent MDCK were infected in replicates with PR8 at an MOI of 10 $TCID_{50}$ /cell, 18-20hpi, 500 µl of the supernatant was collected to re-infect fresh MDCK cells to generate Passage 1. We repeated this for 72 times. From the remaining supernatant of each passage, 140 µl was used for RNA extraction using QIAGEN QIAamp viral RNA mini kit according to the manufacturer's instructions, which was kept, with the rest of the supernatant at -70°C. A fixed-volume blind passaging approach was used throughout all experiments: following the initial high-MOI infection, subsequent passages were performed by transferring a constant volume of supernatant to fresh cells, allowing the effective MOI to fluctuate dynamically across passages.

**Viral cDNA amplification and sequencing.**

Universal RT-PCR was performed on all the samples before sequencing on Illumina MiSeq or NovaSeq using a previously described method [6]. For RT-qPCR quantification of DI250, DI143, DI289 and *PB2*-WT gene segments, we designed and optimized specific primer/probe sets specific for each species using the IDT PrimerQuest webtool and validated efficiency and specificity using serial dilutions of plasmids encoding either species **(Fig S4 & Table S1)**. Viral RNA was extracted from cells or virions as described above and used to synthesize cDNA using the universal primer and a Verso cDNA synthesis kit (Thermo Scientific). We mixed 3µl of RNA with 8µl of H2O, 4µl of cDNA synthesis buffer, 2µl of dNTP mix (5 mM each), 1µl of universal primer (10 µM), 1µl of RT enhancer, and 1µl of Verso enzyme mix, before incubation for 50 mins at 45°C. After this, 1µl of the cDNA product was mixed with 6µl of H2O, 1µl of forward primers (18 µM), 1 µl of reverse primer (18 µM), 1 µl of specific probe (5 µM), and 10 ml of TaqMan Fast Advanced Master Mix (Thermo Scientific). The qPCR conditions used were as follows: 50°C (2 min) and 95°C (2 min), followed by 40 cycles of 95°C (1 s) and 61°C (20 s) using a qPCR QuantStudio 3 thermocycler. The qPCR in Fig 4&5 was generated using Bio-Rad CFX96 thermocycler.

**Generation of recombinant DIPs and mutation insertion.**

We synthesized (Integrated DNA Technologies, Inc.) and cloned the full-length sequences of the 3 selected *PB2*-derived DelVGs (DI250, DI143, DI289) **(Fig 4 & Fig S4)** into pDZ vectors and transfected them individually along with the WT-encoding versions of the remaining 7 plasmids into PB2-expressing HEK293 cells **(Fig S4)** using a standard eight-plasmid reverse-genetics approach, as previously described [6]. The transfection supernatant was used to infect PB2-expressing MDCK cells (MDCK-PB2) for 48 h to generate a seed stock. After treating with DNase, we assessed the clonality of our DIP stocks by reverse transcription reactions with or without reverse transcriptase (RT), followed by a PCR amplification using specific *PB2* primers **(Fig S4B)**. As expected, we found no product when the RT enzyme was left out, while distinct bands with the expected sizes appeared in the presence of RT, and no WT-derived band was observed. MDCK-PB2 cells were kindly provided by Stefan Pöhlmann and were described previously [36]. For mutation insertion, the Q5 Site-Directed Mutagenesis Kit (New England Biolabs, NEB) was used.

***In vitro* co-passaging and competition assays.**

To co-passage the WT and selected DelVGs **(Fig 4B)**, MDCK cells were co-infected at an MOI of 1 *PB2* gene equivalent per cell for each DIP (total MOI 3) alongside 10 MOI of WT, with infections performed in triplicate. After 1 hour of adsorption at 4°C, the inoculum was removed, cells were washed, and MEM supplemented with FBS was added. Progeny virus was collected at 17–20 hpi, and a fixed volume was used to infect fresh cells. Viral RNA was extracted using

the Qiagen QIAamp Viral RNA Mini Kit, and TaqMan qPCR was performed to quantify viral populations. For the competition assay **(Fig 6B, right panel)**, MDCK cells were co-infected at 0.1 MOI WT with DelVG at a 1:10 WT-to-DelVG ratio based on NP gene equivalents, and progeny was harvested at 48 hpi for plaque assay.

**Sequencing analysis of deletion junctions and data availability.**
Raw sequencing reads were filtered based on quality and lengths and fed into our DI-detection pipeline for DelVG junction detection as previously described [6]. Briefly, to maximize our confidence that the detected DelVGs were not derived from artifacts, we accepted only DelVGs with read support above the cutoff values, which were determined by correlation analysis between two technical replicates, i.e. independent RNA extraction of a couple of samples. Additionally, to account for variabilities between NGS datasets and segments we normalized both the NGS read and distinct junctions counts to $10^6$ mapped reads relative to the total aligned reads. Of note, throughout the analysis we carefully considered both levels of the data, the junction count and the NGS read count/support, with the former speaks more to DelVG production and the latter to DelVG replication.

To measure the WT frequency, we defined the DelVG hotspot occurrences of each segment from our NGS analysis before counting the reads that aligned outside these hotspot regions. Next, we normalized the read counts the same way we did with DelVGs to account for the differences across the NGS datasets. We validated this method by using simulated NGS datasets from our previous study that were derived from Cal07 and contained a defined proportion of DelVG and WT reads [6], and found no significant difference between the expected and observed in three different libraries contain different amount of DelVG junctions **(Fig S7)**. To profile mutations in DelVGs, we leveraged their short length and junction placement, which are typically fully covered by ~250-nt reads. Using DelVG sequences as references, we extracted reads spanning the deletion junction and required ≥100 nt of coverage on both sides before conducting variant analysis.

Finally, the mutations were analyzed using LowFreq [37] and SNPGenie [38], and then visualized using circle packing layouts implemented with igraph and ggraph packages in R, enabling comparative analysis of mutation distributions across DI lineages and WT populations.

**Shannon Diversity**
The probability of each DelVG was calculated by dividing the NGS read support of each DleVG by the total DelVG reads, before applying the following equation to calculate the diversity of each population. Shannon Diversity takes into consideration both the NGS and junction counts; the higher the value the higher the diversity.

$$\mathrm{H(X)} = -\sum_{i=0}^{n-1} P_i ln P_i$$

**Minigenome replicon**

HEK293T cells were seeded at 1.5 × $10^5$ cells per well in 24-well plates. After 24 hours, the cells were co-transfected using PolyPlus JetPrime with plasmids encoding the influenza PR8 replication machinery proteins, along with pCI-NP and two additional plasmids: pPolI-Firefly, which expresses the Firefly luciferase coding sequence in negative polarity flanked by the 5′

and 3′ non-coding regions of the NS segment, and pTK-Renilla, driven by a cellular promoter. All plasmids were generously provided by Nadia Naffakh and have been previously described [39]. Six hours post-transfection, the medium was replaced with fresh medium containing 10% FBS and 1% Pen/Strep. After 24 hours of incubation at 37°C, luciferase activity was measured using the Renilla Luciferase Assay System (Promega) and a GloMax luminometer.

**The hemagglutination (HA) assay**

The HA assay was performed in a round-bottom 96-well plate. Serial two-fold dilutions of the virus samples were prepared in PBS (+/+) to a final volume of 50 µL per well, including virus-free negative controls. Turkey red blood cells (RBCs) were washed by resuspending them in 15 mL of PBS (+/+) in a 15 mL conical tube, followed by centrifugation at 1,000 × g for 5 minutes. The supernatant was discarded, and the RBCs were resuspended to a final concentration of 1%. Next, 50 µL of the 1% RBC suspension was added to each well, and the plates were incubated at 4°C for 30–60 minutes. The endpoint dilution showing complete hemagglutination was recorded.

**DI nomenclature**

In this study we follow the nomenclature introduced by Dimmock and Easton [14], where defective interfering (DI) RNAs are designated by the segment of origin and the length of the sequence retained from the 3′ end of the positive-sense RNA before the internal deletion. For example, the prototype DI244 (also written as DI 1/244) derives from segment 1 (*PB2*) and retains the first 244 nucleotides from the 3′ end of the positive strand, together with the terminal nucleotides from the 5′ end, thereby defining the breakpoints of the internal deletion.

**Data availability**

Sequencing data generated in this study are available at NCBI under accession number PRJNA1366758. A Source Data Excel file is provided with this paper, containing multiple sheets with the underlying data and calculations for each figure.

**Code availability**

Custom scripts used for DelVG identification, analysis, and visualization are available at GitHub and archived at Zenodo:
https://doi.org/10.5281/zenodo.20421313.

**References**

1. Brooke, C. B. Population Diversity and Collective Interactions during Influenza Virus Infection. *J Virol* **91**, e01164-17, e01164-17 (2017).

2. Alnaji, F. G. & Brooke, C. B. Influenza virus DI particles: Defective interfering or delightfully interesting? *PLoS Pathog* **16**, e1008436 (2020).

3. Vignuzzi, M. & López, C. B. Defective viral genomes are key drivers of the virus-host interaction. *Nat Microbiol* https://doi.org/10.1038/s41564-019-0465-y (2019) doi:10.1038/s41564-019-0465-y.
4. von Magnus, P. Incomplete Forms of Influenza Virus. in *Advances in Virus Research* (eds Smith, K. M. & Lauffer, M. A.) vol. 2 59–79 (Academic Press, 1954).
5. Janda, J. M., Davis, A. R., Nayak, D. P. & De, B. K. Diversity and generation of defective interfering influenza virus particles. *Virology* **95**, 48–58 (1979).
6. Alnaji, F. G. *et al.* Sequencing Framework for the Sensitive Detection and Precise Mapping of Defective Interfering Particle-Associated Deletions across Influenza A and B Viruses. *J. Virol.* **93**, (2019).
7. Penn, R. *et al.* Levels of Influenza A Virus Defective Viral Genomes Determine Pathogenesis in the BALB/c Mouse Model. *J Virol* **96**, e0117822 (2022).
8. Russell, A. B., Elshina, E., Kowalsky, J. R., Te Velthuis, A. J. W. & Bloom, J. D. Single-cell virus sequencing of influenza infections that trigger innate immunity. *J. Virol.* https://doi.org/10.1128/JVI.00500-19 (2019) doi:10.1128/JVI.00500-19.
9. Lui, W.-Y. *et al.* SMRT sequencing revealed the diversity and characteristics of defective interfering RNAs in influenza A (H7N9) virus infection. *Emerg Microbes Infect* **8**, 662–674 (2019).
10. Saira, K. *et al.* Sequence Analysis of In Vivo Defective Interfering-Like RNA of Influenza A H1N1 Pandemic Virus. *Journal of Virology* **87**, 8064–8074 (2013).
11. Martin, M. A., Kaul, D., Tan, G. S., Woods, C. W. & Koelle, K. The Dynamics of Influenza A H3N2 Defective Viral Genomes from a Human Challenge Study. *bioRxiv* https://doi.org/10.1101/814673 (2019) doi:10.1101/814673.

12. Vasilijevic, J. *et al.* Reduced accumulation of defective viral genomes contributes to severe outcome in influenza virus infected patients. *PLOS Pathogens* **13**, e1006650 (2017).
13. Gard, S. & von Magnus, P. *Studies on Interference in Experimental Influenza: Purification and Centrifugation Experiments / By Svend Gard ; Preben von Magnus*. (Almqvist & Wiksell, 1947).
14. Meng, B. *et al.* Unexpected complexity in the interference activity of a cloned influenza defective interfering RNA. *Virol. J.* **14**, 138 (2017).
15. Duhaut, S. D. & McCauley, J. W. Defective RNAs inhibit the assembly of influenza virus genome segments in a segment-specific manner. *Virology* **216**, 326–337 (1996).
16. Dimmock, N. J. & Easton, A. J. Cloned Defective Interfering Influenza RNA and a Possible Pan-Specific Treatment of Respiratory Virus Diseases. *Viruses* **7**, 3768–3788 (2015).
17. Baum, A., Sachidanandam, R. & García-Sastre, A. Preference of RIG-I for short viral RNA molecules in infected cells revealed by next-generation sequencing. *Proc. Natl. Acad. Sci. U.S.A.* **107**, 16303–16308 (2010).
18. Alnaji, F. G., Reiser, W. K., Rivera-Cardona, J., Te Velthuis, A. J. W. & Brooke, C. B. Influenza A Virus Defective Viral Genomes Are Inefficiently Packaged into Virions Relative to Wild-Type Genomic RNAs. *mBio* **12**, e0295921 (2021).
19. Pelz, L. *et al.* Semi-continuous Propagation of Influenza A Virus and Its Defective Interfering Particles: Analyzing the Dynamic Competition To Select Candidates for Antiviral Therapy. *J Virol* **95**, e01174-21 (2021).
20. Davis, A. R. & Nayak, D. P. Sequence relationships among defective interfering influenza viral RNAs. *Proc Natl Acad Sci U S A* **76**, 3092–3096 (1979).
21. Mendes, M. & Russell, A. B. Library-based analysis reveals segment and length dependent characteristics of defective influenza genomes. *PLoS Pathog* **17**, e1010125 (2021).

22. Ranum, J. N. *et al.* Cryptic proteins translated from deletion-containing viral genomes dramatically expand the influenza virus proteome. *Nucleic Acids Res* **52**, 3199–3212 (2024).
23. Brooke, C. B. *et al.* Most Influenza A Virions Fail To Express at Least One Essential Viral Protein. *Journal of Virology* **87**, 3155–3162 (2013).
24. Laske, T., Heldt, F. S., Hoffmann, H., Frensing, T. & Reichl, U. Reprint of "Modeling the intracellular replication of influenza A virus in the presence of defective interfering RNAs. *Virus Res* **218**, 86–95 (2016).
25. Rüdiger, D., Pelz, L., Hein, M. D., Kupke, S. Y. & Reichl, U. Multiscale model of defective interfering particle replication for influenza A virus infection in animal cell culture. *PLoS Comput Biol* **17**, e1009357 (2021).
26. Vargas-Maldonado, N. *et al.* Controlled human influenza infection reveals heterogeneous expulsion of infectious virus into air. *Cell* S0092867426002321 (2026) doi:10.1016/j.cell.2026.02.025.
27. Xue, K. S. *et al.* Parallel evolution of influenza across multiple spatiotemporal scales. *eLife* **6**, (2017).
28. Xiao, Y. *et al.* A defective viral genome strategy elicits broad protective immunity against respiratory viruses. *Cell* **184**, 6037-6051.e14 (2021).
29. Levi, L. I. *et al.* Defective viral genomes from chikungunya virus are broad-spectrum antivirals and prevent virus dissemination in mosquitoes. *PLOS Pathogens* **17**, e1009110 (2021).
30. Rezelj, V. V. *et al.* Defective viral genomes as therapeutic interfering particles against flavivirus infection in mammalian and mosquito hosts. *Nat Commun* **12**, 2290 (2021).

31. Sanchez David, R. Y. *et al.* Comparative analysis of viral RNA signatures on different RIG-I-like receptors. *eLife* **5**, e11275 (2016).
32. White, K. A. & Morris, T. J. Nonhomologous RNA recombination in tombusviruses: generation and evolution of defective interfering RNAs by stepwise deletions. *J Virol* **68**, 14–24 (1994).
33. Havelda, Z., Burgy√°n, J. & Dalmay, T. Secondary structure-dependent evolution of Cymbidium ringspot virus defective interfering RNA. *Journal of General Virology* **78**, 1227–1234 (1997).
34. Ray, D. & White, K. A. An Internally Located RNA Hairpin Enhances Replication of *Tomato Bushy Stunt Virus* RNAs. *J Virol* **77**, 245–257 (2003).
35. Fodor, E. *et al.* Rescue of influenza A virus from recombinant DNA. *J Virol* **73**, 9679–9682 (1999).
36. Bdeir, N. *et al.* A system for production of defective interfering particles in the absence of infectious influenza A virus. *PLoS ONE* **14**, e0212757 (2019).
37. Wilm, A. *et al.* LoFreq: a sequence-quality aware, ultra-sensitive variant caller for uncovering cell-population heterogeneity from high-throughput sequencing datasets. *Nucleic Acids Res* **40**, 11189–11201 (2012).
38. Nelson, C. W., Moncla, L. H. & Hughes, A. L. SNPGenie: estimating evolutionary parameters to detect natural selection using pooled next-generation sequencing data. *Bioinformatics* **31**, 3709–3711 (2015).
39. Chen, K.-Y., Santos Afonso, E. D., Enouf, V., Isel, C. & Naffakh, N. Influenza virus polymerase subunits co-evolve to ensure proper levels of dimerization of the heterotrimer. *PLoS Pathog* **15**, e1008034 (2019).

**Acknowledgements**
We thank the members of the Brooke and Vignuzzi laboratories for helpful discussions, insightful comments, and continued support throughout this work.

**Funding**
F.G.A., C.B.B., and M.V. disclose support for the research of this work from the Defense Advanced Research Projects Agency (DARPA) under contract DARPA-16-35-INTERCEPT-FP-018, the National Institutes of Health under grants R01AI139246, R01AI179910, and U01AI186993, and the Agency for Science, Technology and Research (ASTAR), Infectious Diseases Labs (IDL), Singapore. F.G.A. and M.V. further disclose support for experiments performed at ASTAR from the National Research Foundation, Singapore [grant number NRF-NRFI08-2022-0005], and the Singapore Therapeutics Development Review (STDR) programme [grant number H25G1a0177]. The remaining authors declare no relevant funding.

**Author's contributions**
F.G.A. designed and performed experiments, developed the major DelVG detection pipeline, performed bioinformatics analyses, analyzed deep sequencing data, developed data visualization concepts, and contributed to manuscript writing. M.F. performed competitive WT and DelVG experiments. S.L.G. and D.Z.H.A. quantified WT and DelVG populations in passaging experiments. T.L. contributed to streamplot development and visualization. P.A.L. and R.C.L.-Z. contributed to the development of circle-packing visualizations. C.L. assisted in optimization of the minigenome replicon system. M.V. supervised the project at A*STAR. C.B.B. supervised the project at the University of Illinois Urbana-Champaign. F.G.A., M.V., and C.B.B. wrote the manuscript. All authors reviewed and approved the final manuscript.

**Competing interests**
The Authors declare the following competing interests. F.G.A., M.V., and C.B.B. are inventors on a provisional patent application related to therapeutic defective interfering particles and based in part on work presented in this study (U.S. provisional patent application no. 63/903,970). The remaining authors declare no competing interests.

**Figure Legends:**

***Fig 1. NGS-based analysis of DelVG dynamics across genomic segments during serial passaging**. **(A)** Particle-to-infectivity ratios across passages in two independently passaged lineages (L1 & L2). Physical particle counts were quantified by hemagglutination (HA) assay and normalized to infectivity measured by $TCID_{50}$. **(B)** Segment-resolved DelVG dynamics across selected passages are shown as junction counts and NGS-derived read frequencies for all eight viral segments in both lineages. Both metrics were normalized per $10^6$ mapped reads using the total number of reads aligned to each segment. Lineage colors are as in (A). "Seed" denotes the parental virus population used to initiate each lineage **(C)** Heatmap of PB2-derived DelVG proportional abundance (%) across eight independent lineages (L1, L2, and six additional replicates). Each row represents a unique deletion junction, and columns indicate relative abundance across lineages. Only DelVGs reaching ≥5% abundance in at least one lineage were included. White cells indicate absence of the junction in a given lineage. Theoretical minimum and maximum abundance values are indicated for reference. Source data are provided as a Source Data file.*

***Fig 2. Longitudinal changes in WT:DelVG ratios and DelVG diversity across polymerase segments.*** *WT and DelVG proportions were quantified across serial passages for the polymerase segments PB2, PB1, and PA in both lineages. Stacked bars show the relative contribution of WT-derived reads and DelVG-derived reads for the polymerase segments at each passage, expressed as the WT/DelVG ratio (%). WT reads are shown in grey, while DelVG reads are shown in lineage-specific colors: burgundy red for L1 and cerulean blue for L2. The black line and points show Shannon diversity of DelVG populations at the corresponding passages, calculated from the relative abundance of distinct DelVG junctions within each segment. Source data are provided as a Source Data file.*

***Fig 3. Emergence of dominant junctions during passaging.*** *Streamplots depicting DelVG population dynamics across passages for each influenza genome segment in both lineages. DelVG read counts were normalized to $10^6$ mapped reads before plotting. Each row represents one segment, and each colored stream represents a distinct segment-derived DelVG, with stream thickness reflecting the abundance of that DelVG at each passage. For visualization, low-abundance DelVGs were distributed to the upper and lower layers of each streamplot, whereas higher-abundance/selected DelVGs were positioned centrally. Colors are assigned independently per plot; identical colors across segments do not denote the same DelVG. Source data are provided as a Source Data file.*

***Fig 4. Competitive dynamics of clonal PB2-derived DelVGs during serial passage. (A)*** *The PB2_L1 streamplot from Fig 3 was modified to highlight three selected DelVGs, while all other DelVGs were rendered in white/background. The highlighted DelVGs are shown in purple (DI250), blue (DI143), and red (DI289). The right panel shows the junction location of each highlighted DelVG along the PB2 segment, together with the corresponding DelVG size. DI289 was outcompeted early during passaging and is therefore less visually prominent, appearing only as a small red trace near the left side of the streamplot. An arrow was added to point toward DI289 trace and aid visualization.* ***(B)*** *Competition assays of clonal DIPs during serial passaging. MDCK cells were co-infected with DI250, DI143, and DI289 at equal input levels (MOI = 1 each, based on PB2 gene equivalents; total MOI = 3), together with WT virus (MOI = 10), and passaged for 16 passages. Viral dynamics were quantified by RT-qPCR as PB2 copy number ($log_{10}$ copies / µl) across three independent replicates. Source data are provided as a Source Data file.*

***Fig 5. NGS-based analysis of mutation frequencies in WT and DelVG populations across passages.*** *Circle-packing diagrams showing the frequency and distribution of single-nucleotide polymorphisms (SNPs) across passages in WT virus and dominant DelVGs from both lineages. Each circle represents a distinct SNP, with circle size proportional to its frequency within the population. Passages are indicated for each lineage, with "Seed" denoting the parental virus population used to initiate passaging. Highlighted circles indicate selected high-frequency mutations, with WT-associated mutations shown in light green and DelVG-associated mutations in pink. The most frequent mutations are annotated, including A1414G in WT populations and A94G, which emerges specifically in PB2-derived DelVGs. Source data are provided as a Source Data file.*

***Fig 6. Functional characterization of the A94G mutation in WT virus and DelVG contexts. (A)*** *Validation of the A94G mutation in the WT background across passages, assessed by agarose gel electrophoresis, RT–qPCR quantification of PB2 copy number, and Sanger*

*sequencing using PB2-specific primers. The experiment was independently repeated three times with consistent overall results. Reversion of the mutation was observed in one replicate. DNA size markers are indicated for agarose gels. Uncropped gel images are provided in the Source Data file.* ***(B)*** *Functional impact of A94G in DelVG-mediated interference. Left, minigenome replicon assay measuring polymerase activity in the presence of DI250 or DI250:A94G, with pUC19 as a negative control. Right, competition assays between WT virus and clonal DI populations (DI250 or DI250:A94G) using a 1:10 WT:DIP input ratio normalized by NP copy number; viral output was quantified by plaque assay (PFU/mL).. Data are presented as mean values ± SD (n = 3 and n = 5 biological replicates for the minigenome and co-infection assays, respectively). Statistical significance was assessed using a two-tailed t-test. ( P = 0.002 for the minigenome assay and P = 0.016 for the co-infection assay). Source data are provided as a Source Data file. Raw data are provided in the Source Data file.* ***(C)*** *Serial passaging of DI250 and DI250:A94G in 293 cells followed by infection of MDCK cells. Cells were transfected with plasmids expressing both negative- and positive-sense DI RNA, infected 24 h later, and passaged for 14 rounds. The DelVG-to-NP ratio was quantified by RT–qPCR (left), and viral infectivity was measured by* $TCID_{50}$ *(right). Data from a second biological replicate are shown in Fig S5B. Statistical significance is denoted as follows: *P < 0.05, **P < 0.01.*

***Fig 7. Replication and packaging dynamics of DI250 and DI250:A94G****. Clonal DI250 or DI250:A94G populations were co-passaged with WT PR8 for five serial passages in duplicate lineages.* ***(A)*** *DelVG copy numbers across passages, measured by RT–qPCR in intracellular and extracellular fractions.* ***(B)*** *Ratio of DelVG to NP segment across passages.* ***(C)*** *Packaging efficiency of DI250 and DI250:A94G. 293 cells were co-transfected with DI250 and DI250:A94G plasmids at a 1:1 ratio together with the remaining seven PR8 plasmids and a PB2 mRNA-expressing plasmid. After 48 h, supernatants were treated with RNase, followed by RNA extraction, DNase treatment, RT–PCR, and long-read sequencing (Oxford Nanopore). The relative proportion of each DelVG incorporated into virions is shown. Statistical significance was determined using a two-tailed unpaired t-test; ns, not significant (P=0.4). Data are presented as mean values ± SD from three independent replicates. Source data are provided as a Source Data file.*

**Editorial summary:**
Tracking influenza virus populations over 72 passages, the authors show that hundreds of defective viral genomes compete for dominance, ultimately resolving into a single variant carrying an adaptive mutation that enhances replication and interference, enabling it to outcompete other defective genomes.
**Peer review information**: *Nature Communications* thanks Hana Dobrovolny, and the other, anonymous, reviewer(s) for their contribution to the peer review of this work. A peer review file is available.

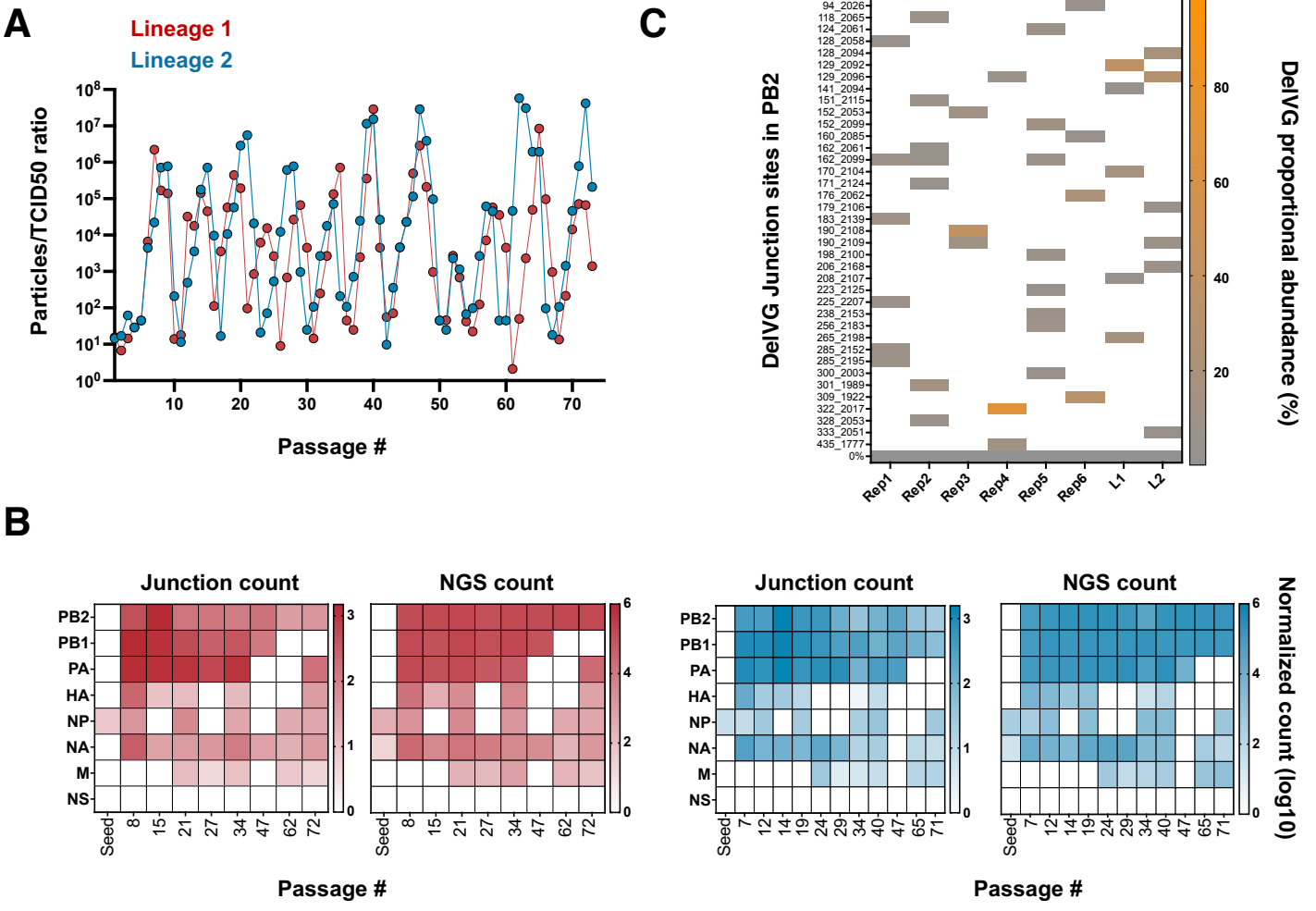
A
Lineage 1
Lineage 2
Particles/TCID50 ratio
Passage #
B
Junction count
NGS count
PB2
PB1
PA
HA
NP
NA
M
NS
Seed
Passage #
Normalized count (log10)
C
DelVG Junction sites in PB2
DelVG proportional abundance (%)
Rep1
Rep2
Rep3
Rep4
Rep5
Rep6
L1
L2

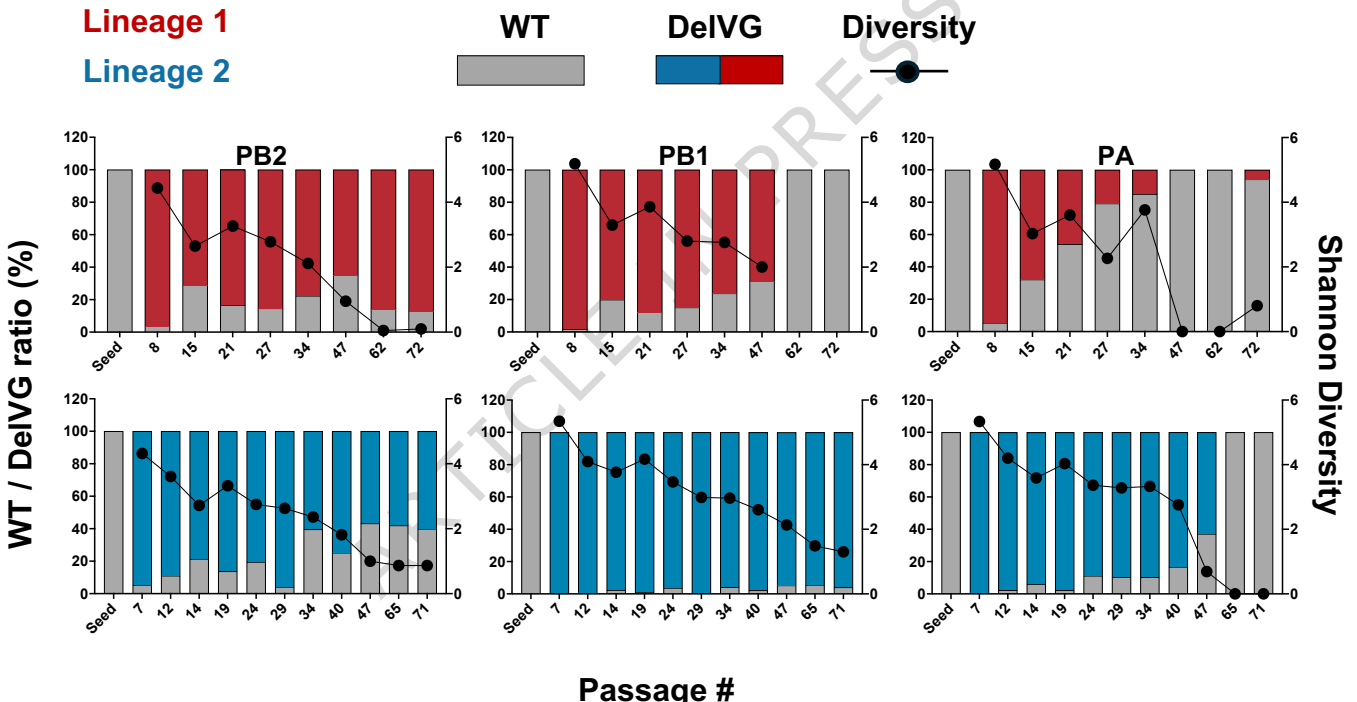

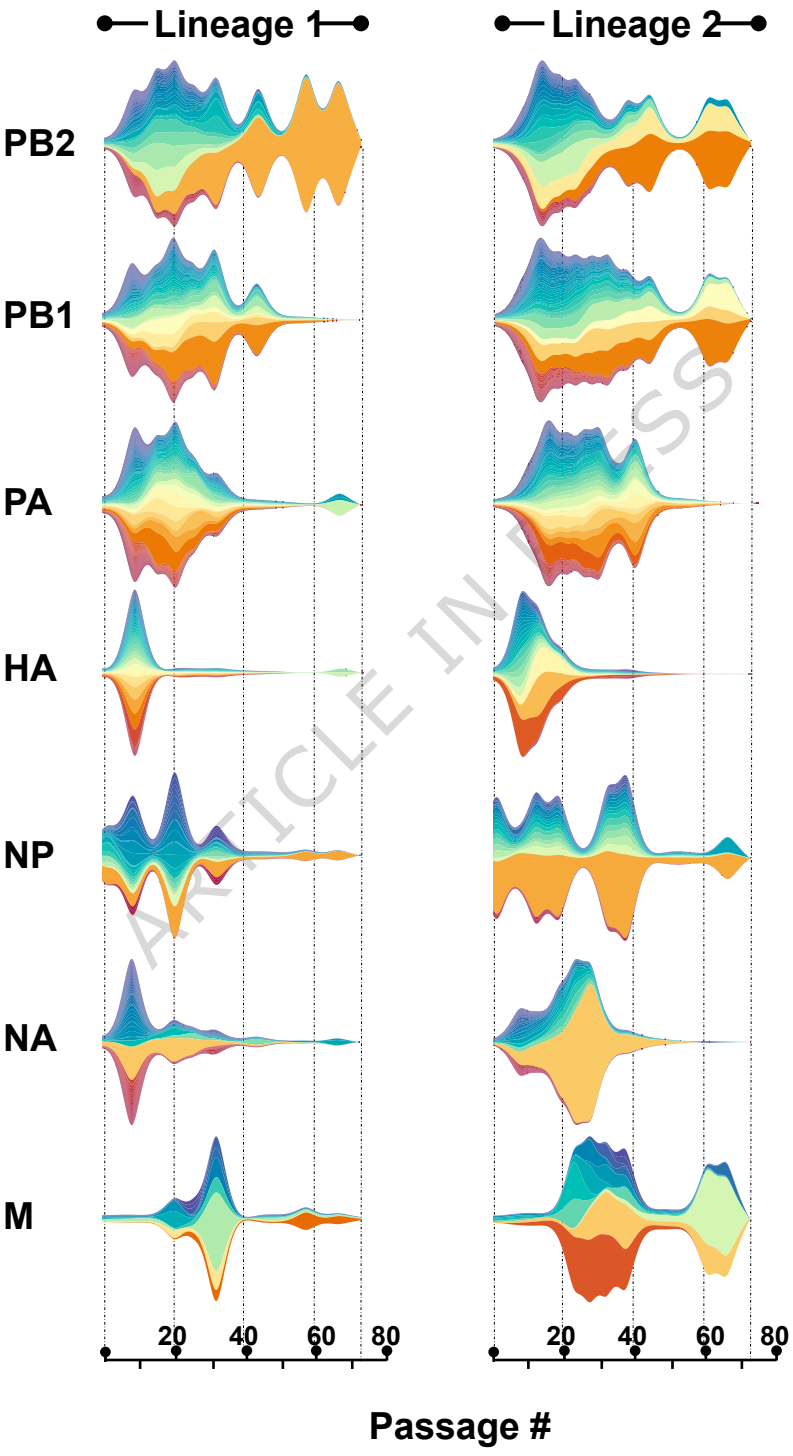

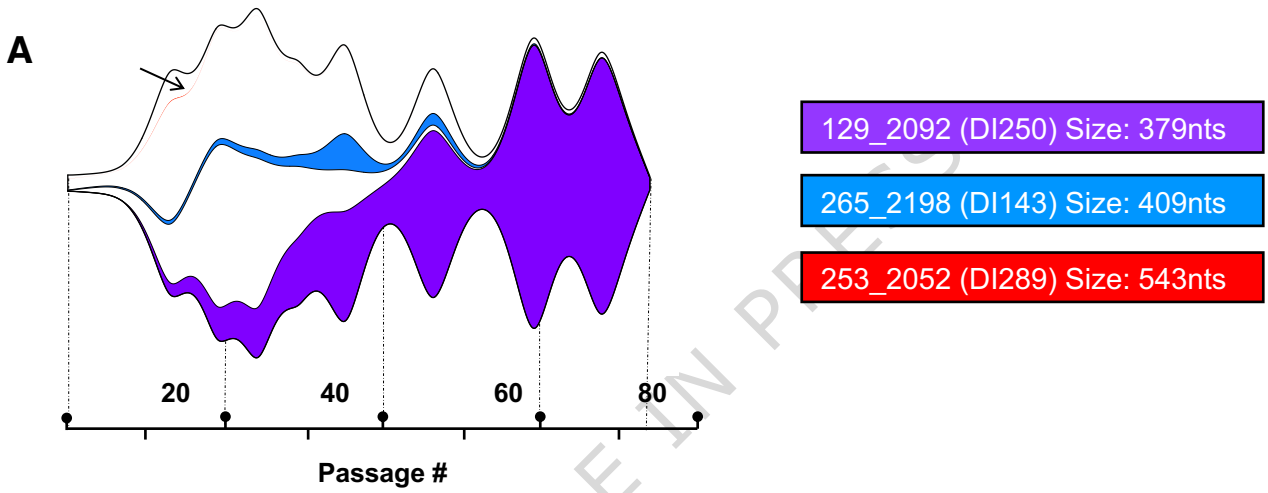
A
20
40
60
80
Passage #
129_2092 (DI250) Size: 379nts
265_2198 (DI143) Size: 409nts
253_2052 (DI289) Size: 543nts

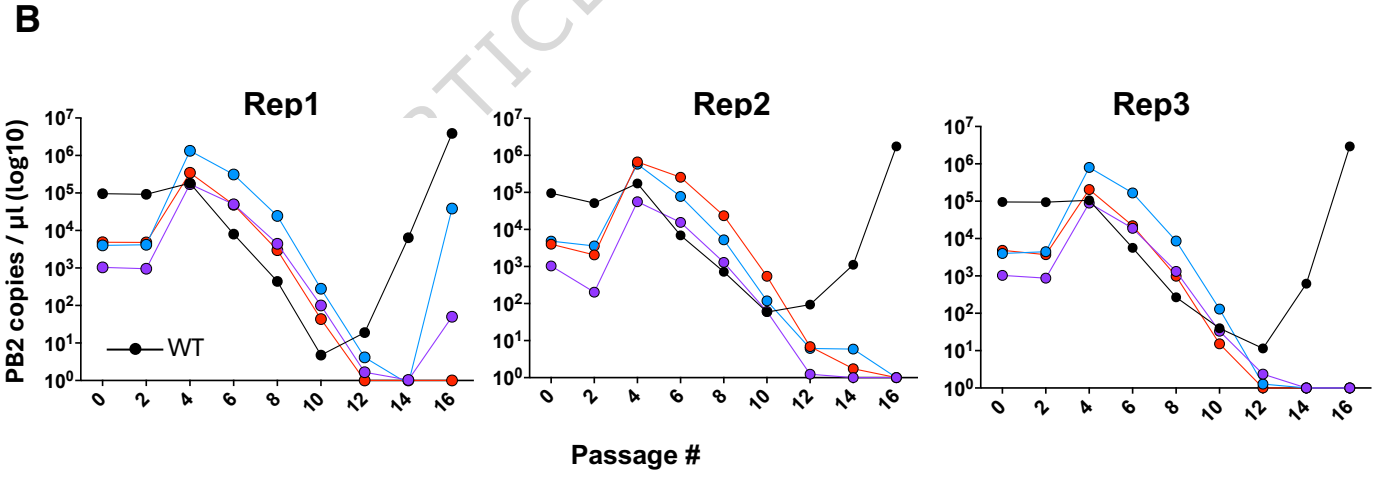
B
Rep1
Rep2
Rep3
PB2 copies / µl (log10)
WT
Passage #